PHOTONICS Research

Thermo-optically tunable spectral broadening in a nonlinear ultra-silicon-rich nitride Bragg grating

Yanmei Cao,[1] Ezgi Sahin,[1,2] Ju Won Choi,[1] Peng Xing,[1] George F. R. Chen,[1] D. K. T. Ng,[3] Benjamin J. Eggleton,[4,5] and Dawn T. H. Tan[1,*]

[1]Photonics Devices and Systems Group, Singapore University of Technology and Design, 8 Somapah Road, Singapore 487372, Singapore
[2]Current address: Photonic Systems Laboratory (PHOSL), Ecole Polytechnique Fédérale de Lausanne, STI-IEL, Station 11, CH-1015 Lausanne, Switzerland
[3]Institute of Microelectronics, A*STAR, 2 Fusionopolis Way, #08-02, Innovis Tower, Singapore 138634, Singapore
[4]Institute of Photonics and Optical Science, School of Physics, The University of Sydney, Sydney, New South Wales 2006, Australia
[5]The University of Sydney Nano Institute (Sydney Nano), The University of Sydney, Sydney, New South Wales 2006, Australia
*Corresponding author: dawn_tan@sutd.edu.sg

Received 28 September 2020; revised 11 January 2021; accepted 3 February 2021; posted 5 February 2021 (Doc. ID 411073); published 31 March 2021

Spectral tunability methods used in optical communications and signal processing leveraging optical, electrical, and acousto-optic effects typically involve spectral truncation that results in energy loss. Here we demonstrate temperature tunable spectral broadening using a nonlinear ultra-silicon-rich nitride device consisting of a 3-mm-long cladding-modulated Bragg grating and a 7-mm-long nonlinear channel waveguide. By operating at frequencies close to the grating band edge, in an apodized Bragg grating, we access strong grating-induced dispersion while maintaining low losses and high transmissivity. We further exploit the redshift in the Bragg grating stopband due to the thermo-optic effect to achieve tunable dispersion, leading to varying degrees of soliton-effect compression and self-phase-modulation-induced spectral broadening. We observe an increase in the bandwidth of the output pulse spectrum from 69 to 106 nm as temperature decreases from 70°C to 25°C, in good agreement with simulated results using the generalized nonlinear Schrödinger equation. The demonstrated approach provides a new avenue to achieve on-chip laser spectral tuning without loss in pulse energy.

https://doi.org/10.1364/PRJ.411073

1. INTRODUCTION

Spectral manipulation of optical pulses is an essential function for lasers used in imaging [1] and precision manufacturing [2]. Tuning the spectral bandwidth of a pulse may be achieved using a variety of methods, including acousto-optic filters [3,4], strain-induced fiber Bragg gratings [5], electro-optic modulators [6], and resonant filters [7–9]. However, many of these methods for pulse spectral tuning involve spectral truncation by band-pass filtering of the pulse. The frequencies that are filtered out cause loss in pulse energy, with the amount of pulse energy loss increasing as the filter bandwidth decreases. For example, spectral tuning of lasers using an acousto-optic filter is an inherently lossy method requiring trunctation of the pulse spectrum to achieve smaller bandwidths. This approach was previously reported to have high losses (close to 20 dB) while allowing a spectral bandwidth tuning dynamic range of less than 2 nm [3,4]. Laser pulse bandwidth tuning has also been demonstrated using strain-induced chirped fiber Bragg gratings (FBGs) [5] and electroabsorption modulators [6], both of which provide a bandwidth tuning dynamic range of less than 1 nm. Bandwidth tuning of laser pulses may also be achieved using passive filters such as mircoring Mach Zehnder interferometers [7], interferometric couplers [8], and microtoroidal resonators [9]. However, similar to the aforementioned methods for pulse bandwidth tuning, these approaches also lead to pulse energy losses from their fundamental operating principle requiring the truncation of the pulse spectrum.

In addition to the loss of pulse energy associated with spectral truncation, the bandwidth tuning dynamic range is relatively narrow, limiting their use in practical applications, such as wavelength division multiplexers [10,11]. A high-performance tuning method that (i) preserves the pulse energy with negligible losses and (ii) provides a wide spectral bandwidth tuning range would be useful for the tuning of the output pulse bandwidth.

Thermally tunable devices offer tunable functionality such as dynamic tuning of wavelength-division multiplexers and continuously tunable oscillators [10–13]. With linear systems, however, the frequency content is defined by the multiplication of the input spectrum and filter shape, which constrains the flexibility to shape the spectrum. Nonlinearities, on the other

hand, allow for the generation of new frequencies, which can be the basis of spectral broadening and spectral shifting and more generally allow for spectral shaping. Generally speaking, the nonlinear shaping dynamics depend on the dispersion properties that are intrinsic to the waveguide [14]. Combining thermal tuning with nonlinearities could provide a pathway for dynamic control of the dispersion, which introduces new degrees of freedom for achieving spectral shaping.

In this paper, we present a method for tuning the spectrum of an optical pulse based on the combination of nonlinear spectral shaping and thermal waveguide tuning. No spectral truncation is required in our laser tuning method, which thus minimizes losses in the pulse energy. We leverage a nonlinear ultra-silicon-rich nitride (USRN) Bragg grating concatenated with a USRN waveguide to achieve thermo-optically tunable spectral broadening. This technique harnesses the thermo-optic effect to redshift the grating stopband as the temperature is increased, leading to tunable dispersion. Since the grating-induced dispersion varies strongly with wavelength detuning from the grating stopband, changes in temperature enable the extent of Bragg soliton-effect compression to be tuned. Importantly, we operate close to the grating band edge (blue side), where transmission is high, and the grating-induced dispersion is large (3 orders of magnitude larger than in waveguides) and anomalous. We experimentally demonstrate an output pulse spectral bandwidth dynamic range from 106 to 69 nm as the temperature is increased from 25°C to 70°C, in good agreement with simulations of the generalized nonlinear Schrödinger equation (GNLSE). This new approach allows pulse bandwidth tuning with minimal energy loss and a wide bandwidth tunability.

2. DEVICE DESIGN AND NUMERICAL SIMULATION OF PULSE PROPAGATION DYNAMICS IN USRN GRATINGS

The 3D schematic of our device is shown in Fig. 1. The USRN device has two stages, consisting of (i) a cladding-apodized modulated Bragg grating (CMBG) with a length of 3 mm and (ii) a 7-mm-long USRN channel waveguide with a width of 550 nm and a height of 300 nm. The CMBG stage consists of a USRN waveguide with pillars placed adjacent to it with a gap. Apodization is implemented by gradually decreasing the gap between the pillars and the central waveguide from the two ends of the grating toward the center according to a raised cosine function, shown in Eq. (1):

$$G(z) = (G_{\text{apod}} - G_1) \times \cos^2(\pi x) + G_1, \text{where}$$
$$x = \begin{cases} \frac{z}{2L_{\text{apod}}}, & \text{if } z \le L_{\text{apod}}, \\ 0.5, & \text{if } L_{\text{apod}} < z \le L_{\text{CMBG}} - L_{\text{apod}}, \\ \frac{z - L_{\text{CMBG}}}{2L_{\text{apod}}}, & \text{if } z > L_{\text{CMBG}} - L_{\text{apod}}, \end{cases} \quad (1)$$

where G_{apod} and G_1 are the gaps between the pillar and the central waveguide at the two ends as well as between the pillar and the center of the CMBG stage, respectively. L_{apod} is the apodization length of 200 μm and L_{CMBG} is the CMBG length of 3 mm. z is the propagation distance of light along the CMBG stage, and $z = 0$ is at the input end of the CMBG.

The apodization scheme used in our work helps to modulate the extent of effective refractive index perturbation and hence gradually increase the coupling strength from almost zero at the input to its maximum at the center and then gradually decrease

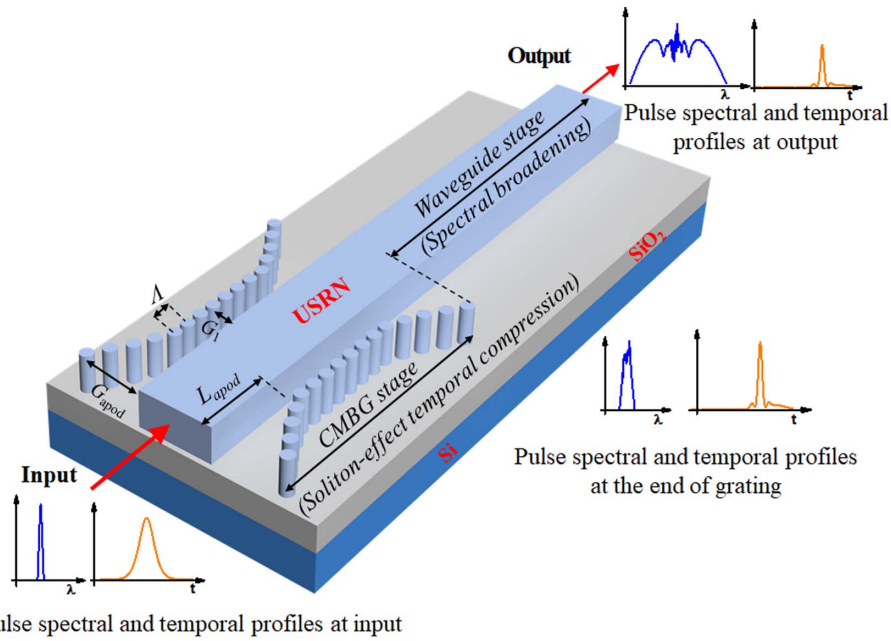

Fig. 1. 3D schematic of the ultra-silicon-rich nitride (USRN) device showing the CMBG and USRN waveguide parameters, where L_{apod} is the apodization length, Λ is the grating pitch, and G_1 and G_{apod} are the distances between the pillars and the USRN waveguide. The insets show the principle of our thermo-optic tuning method.

it to zero at the end of the CMBG stage. The gradual change prevents the optical field from encountering a sudden effective index change at the entrance of the device, minimizing the ripple in the transmission spectrum.

The pillar positioning modulates the effective refractive index seen by the light propagating within the waveguide, whereas the grating pitch is used to tune the spectral position of the stopband. The Bragg grating has a period designed to target a stopband at around 1550 nm.

The principle of our thermo-optic tuning method can be schematically shown by the insets in Fig. 1. When an ultra short pulse is injected into the USRN device, it will experience a temporal compression process in the Bragg grating stage, so the temporal profile at the end of the grating is narrower than that at the input, and it varies with the temperature. Then the pulse further propagates through the nonlinear channel waveguide, and it experiences varying degrees of self-phase-modulation-induced spectral broadening depending on the magnitude of dispersion experienced, so a much broader pulse spectrum is obtained at the output of the two-stage device, and it also varies with the temperature.

We used complementary metal-oxide-semiconductor (CMOS)-compatible USRN as our material platform. The USRN platform has a material composition of Si_7N_3 and large linear and nonlinear refractive indices of 3.1 and 2.8×10^{-13} cm^2 /W, respectively. The nonlinear refractive index, in particular, is 2 orders of magnitude larger than that of stoichiometric silicon nitride. Moreover, the USRN has a large enough band gap of 2.1 eV to preclude two-photon absorption at telecommunications wavelengths [15,16].

The pulse propagation dynamics occurring in the USRN grating is first studied by solving the generalized nonlinear Schrödinger equation (GNLSE), assuming a slowly varying pulse envelope $A(z,t)$, which is a good approximation in this regime, via the split-step Fourier method:

$$\frac{\partial A}{\partial z} = \sum_{k=2}^{4} \frac{i^{k+1}}{k!} \beta_k \frac{\partial^k A}{\partial t^k} - \frac{\alpha}{2} A + i\gamma_{\text{eff}}(|A|^2 A). \tag{2}$$

The initial input pulse $A(0,t)$ is assumed to have an unchirped hyperbolic-secant field profile, with peak power $P_0 = 4.7$ W and a center wavelength of 1536 nm. The input pulses modeled in the simulation have the same parameters as that used in the experiment.

Contributions of dispersion to pulse propagation are included through the first term on the right-hand side, where β_k denotes the kth-order dispersion. The last term of Eq. (2) takes self-phase modulation (SPM) into account, and γ_{eff} denotes the effective nonlinear parameter.

We simulate the two stages comprising (i) the cladding-apodized modulated Bragg grating and (ii) the USRN channel waveguide. In the first stage simulation, we used the same parameters as the Bragg grating stage of our device used in the experiment, such as the propagation length of 3 mm, the dispersion coefficients, and the effective nonlinear parameter of the Bragg grating stage of our device. In the second stage simulation, we used the same parameters as the USRN waveguide stage of our device used in the experiment, such as the propagation length of 7 mm, the dispersion coefficients, and the effective nonlinear parameter of the USRN waveguide stage of our device.

The role of the Bragg grating is to first create soliton-effect temporal compression. Optical solitons leverage the balance between dispersion and nonlinearity to propagate long distances with minimal changes in their shape. When the nonlinearity is stronger than dispersion, high-order solitons may be supported and undergo soliton-effect compression and fission when large higher-order dispersion is present. The Bragg grating dispersion has previously been shown to be 3 orders of magnitude larger than that in photonic waveguides [17], a feature that is fundamental to the observation of Bragg soliton-effect compression in the Bragg grating. The magnitude of anomalous dispersion (on the blue side of the grating band edge) was further shown to be strongly wavelength dependent, with the magnitude decreasing as one moves futher away from the grating stopband.

At the end of the Bragg grating, the pulse has undergone some degree of Bragg soliton-effect compression, depending on the detuning of the pulse from the stopband, and it therefore possesses an increased peak power and reduced temporal pulse width prior to propagating in the USRN waveguide. Enhanced self-phase-modulation-induced spectral broadening then occurs in the waveguide as a result of the shorter pulse width and higher peak power. For the Bragg grating stage, γ_{eff} is calculated as $\gamma_{\text{eff}} = [(\omega_0 n_2)/(cA_{\text{eff}})] \times (n_g/n_0)^2$, where ω_0 is the frequency of the initial input pulse, n_g is the group index, and n_0 is the refractive index of the USRN material. The effective mode area A_{eff} is calculated using the finite element method to be 0.24 μm^2. The values for group index n_g and the second- to fourth-order dispersion coefficients ($\beta_{2,3,4}$) as a function of temperature are shown in Fig. 2, and they are obtained through experiment. It may be observed that the magnitude of $\beta_{2,3,4}$ is highest at the lowest temperature of 25°C. β_2, in particular, is anomalous and affects the soliton order according to the equation $N^2 = L_D/L_{\text{NL}} = T_0^2 \gamma_{\text{eff}} P_0/|\beta_2(T)|$, where $T_0 = T_{\text{FWHM}}/1.76$, T_{FWHM} is the pulse full width at half-maximum (FWHM), P_0 is the pulse peak power, and $\beta_2(T)$ is the temperature (T)-dependent second-order dispersion. Consequently, for a fixed T, the soliton order may be varied by changing P_0. As T is increased, the magnitude of $\beta_2(T)$ decreases and results in higher soliton orders. The soliton period is further defined as $z_0 = \pi/2 \times T_0/|\beta_2(T)|$, implying that a larger soliton order arising from a larger magnitude of $\beta_2(T)$ will also increase the soliton period.

For the second simulation stage, γ_{eff} for the USRN waveguide is defined as $\gamma_{\text{eff}} = (\omega_0 n_2)/(cA_{\text{eff}})$. The dispersion coefficients of the waveguide are 3 orders of magnitude smaller than in the grating. We only consider the second-order dispersion effect with a value of -0.1 ps^2/m, the same as the experimental value. Nonlinear losses have been shown to be negligible at optical intensities up to 50 GW/cm^2 for the USRN platform [18], significantly larger than the power levels used in this simulation. Therefore, we only take the linear propagation loss α into account. We used the experimentally obtained propagation losses for the first- and second-stage simulations, which are 13 dB/cm and 3.5 dB/cm, respectively [17].

The temperature-dependent output pulse spectrum is studied using numerical simulations, and the results are shown in

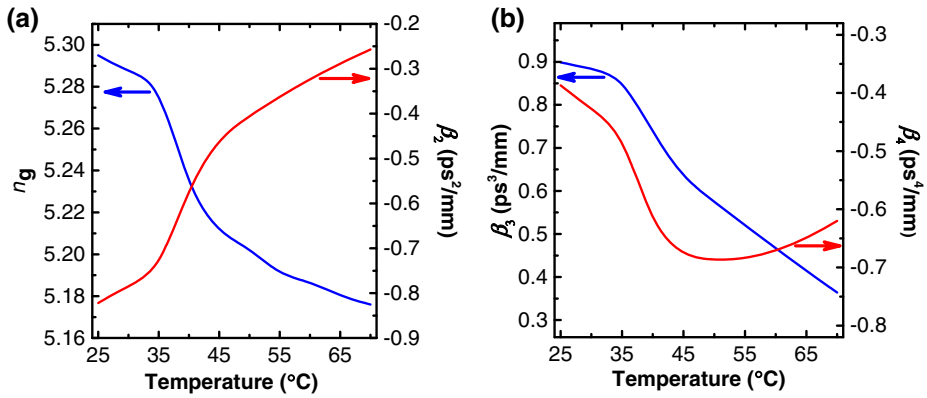

Fig. 2. (a) Group index (n_g) and second-order dispersion (β_2) coefficient of the CMBG at different temperatures located at 1536 nm. (b) Third-order (β_3) and fourth-order dispersion (β_4) coefficients of the CMBG at different temperatures located at 1536 nm.

Figs. 3(a)–3(c). Figure 3(a) shows the spectral broadening at several different temperatures. Based on the raw data in Fig. 3(a), we further calculated the spectral bandwidth at the −30 dB and −20 dB level plotted in Figs. 3(b) and 3(c), respectively, showing a good overall agreement with the experimentally observed trends. It can be seen that the bandwidth decreases as the temperature is increased from 25°C to 70°C. Enhancement in the spectral broadening when pulses are located close to the grating stopband is evaluated to arise because of (i) a slower group velocity overall and (ii) strong anomalous dispersion, which provides varying degrees of soliton-effect compression. The augmented group index leads to a moderate slow-light enhancement in the nonlinear effect. Soliton-effect compression occurs in the grating structure, with the compression effect being strongest at the baseline temperature of 25°C, where the pulse is situated closest to the stopband of the grating.

Though our experimental setup was limited to a minimum temperature of 25°C, we expect that at temperatures below 25°C the pulse will be situated even closer to the grating stopband, leading to stronger soliton-effect compression. As shown in Fig. 4(c), the numerically calculated temporal compression effect in the CMBG stage continues to strengthen below 25°C.

Soliton-effect compression arises as a result of the strong anomalous dispersion and the high nonlinearity from the USRN and the grating structure, with the compression effect being strongest at a temperature of 25°C, where the pulse is situated closest to the stopband of the grating. To further elucidate the role of soliton-effect compression, we simulated the spectral [Fig. 4(a)] and temporal profiles [Fig. 4(b)] of the pulse at the end of the Bragg grating stage as the temperature is increased from 15°C to 70°C. From Fig. 4(b), it is observed that within a range of temperature from 25°C to 70°C, Bragg soliton-effect temporal compression is occurring, with the shortest pulse width occurring when the temperature is 25°C. This is accompanied by a pulse with the highest spectral content. The temporal FWHM as a function of temperature with a broader range is further shown in Fig. 4(c), where it is observed that temporal pulse width gradually increases with temperature. Therefore, the extent of Bragg soliton-effect compression decreases with the increasing temperature, and this will result in a decrease in the amount of spectral broadening that can

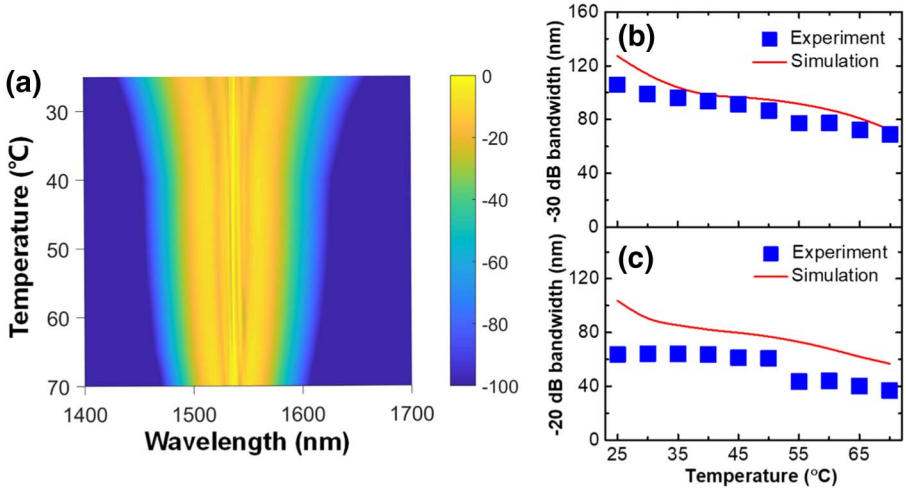

Fig. 3. (a) Simulated spectral broadening at different temperatures at a fixed pulse wavelength of 1536 nm. Simulated and measured (b) −30 dB and (c) −20 dB bandwidth of the output spectrum as a function of temperature.

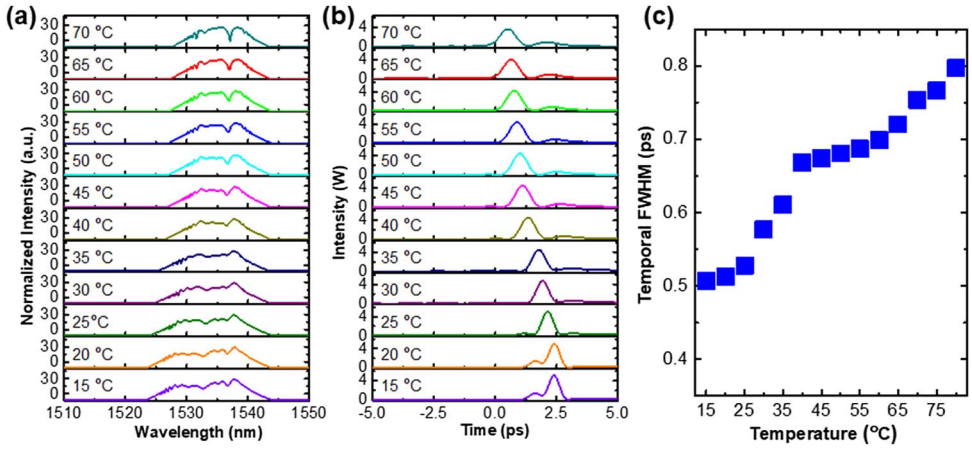

Fig. 4. (a) Simulated spectral profiles at the end of the CMBG. (b) Simulated temporal profiles as a function of temperature at the end of the CMBG. (c) Simulated temporal FWHM at the end of the CMBG stage for each temperature point.

occur in the USRN waveguide. In addition, the compressed pulse peak power is also highest at 25°C, which further contributes to the increased spectral broadening in the USRN waveguide as the temperature is decreased from 70°C to 25°C.

3. DEVICE FABRICATION AND EXPERIMENTAL CHARACTERIZATION

Our devices are fabricated on a silicon substrate with a 10 μm SiO_2 thermal oxide layer. The USRN film is first deposited using inductively coupled chemical vapor deposition at a low temperature of 250°C. The grating-waveguide structures were first defined using electron-beam lithography. Inductively coupled plasma etching was used to transfer the mask pattern to the USRN layer. Finally, 2 μm SiO_2 cladding deposition was performed using atomic layer deposition and plasma-enhanced vapor deposition.

The schematic of our experimental setup for demonstrating thermally tunable spectral broadening is shown in Fig. 5(a). In the experiment, we utilized a mode-locked femtosecond fiber laser, which is wavelength tunable and emits hyperbolic-secant pulses. The pulses have an FWHM of ~2 ps at a repetition rate of 20 MHz, and they are adjusted for quasi-TE polarization before coupling into the waveguide device using tapered fibers. The wavelength of the input pulses was set at 1536 nm, and the coupled average power entering the waveguide device was fixed at 0.2 mW, the same power level as a peak power of 4.7 W used in the simulation. To characterize the output spectrum, we used an optical spectrum analyzer (OSA) with a measurement range from 1400 to 1650 nm. The device was placed directly on a heater controlled by a temperature controller, and the temperature was varied from 25°C to 70°C at 5°C intervals.

Enhanced temporal compression is expected to occur at a lower temperature. As shown in Fig. 4(c), the temporal compression effect in the CMBG stage is stronger for a lower temperature (below 25°C). However, the lowest temperature our experiment could go to was 25°C, as we were using a heater controlled by a temperature controller, which can increase the temperature but not decrease the temperature below room temperature. Consequently, we could only investigate the trend above 25°C experimentally.

When a laser pulse with a wavelength close to the blue side of the grating band edge is injected into a Bragg grating, it experiences large anomalous dispersion, resulting in Bragg soliton-effect temporal compression. Subsequently, the temporal compression of pulses will enhance the spectral broadening in the USRN waveguide by increasing the peak power and/or expanding the spectral content prior to the pulse entering the waveguide.

The output pulse spectra were measured using an OSA, and the results are shown in Figs. 5(b) and 5(c). Figure 5(b) shows the transmission spectrum of the device with a fixed input pulse wavelength of 1536 nm. The output pulse spectrum is experimentally observed to get narrower as the temperature increases from 25°C to 70°C. Furthermore, we calculated the spectral bandwidth at the −30 dB level based on the spectrum measured in Fig. 5(b), which is summarized and plotted in Fig. 5(c). It is observed that the −30 dB bandwidth decreases from 106 to 69 nm when the temperature is increased from 25°C to 70°C.

We further measured the transmission spectra of another USRN grating with a broadband amplified spontaneous emission (ASE) source, at the same temperature points, as shown in Fig. 6(a). This new USRN grating has the same structure as the device used in the spectral broadening measurement, but with a different grating pitch. As observed in Fig. 6(a), the stopband of this new grating is centered at 1557 nm at 25°C, and there is a redshift in the stopband as the temperature is increased from 25°C to 70°C.

Transmission characteristics of the USRN grating used in the spectral broadening measurement are shown in Fig. 6(b), where it is observed that the grating's stopband is centered at a wavelength of 1553 nm at 25°C. The total device loss from the grating and USRN waveguide is around 6 dB near the blue-side edge of the stopband, a relatively low loss level. Consequently, the input pulses centered at 1536 nm operate at the high transmission wavelength region of the Bragg grating, which is important for power-efficient short pulse dynamics in nonlinear media. By now, we can reach the following

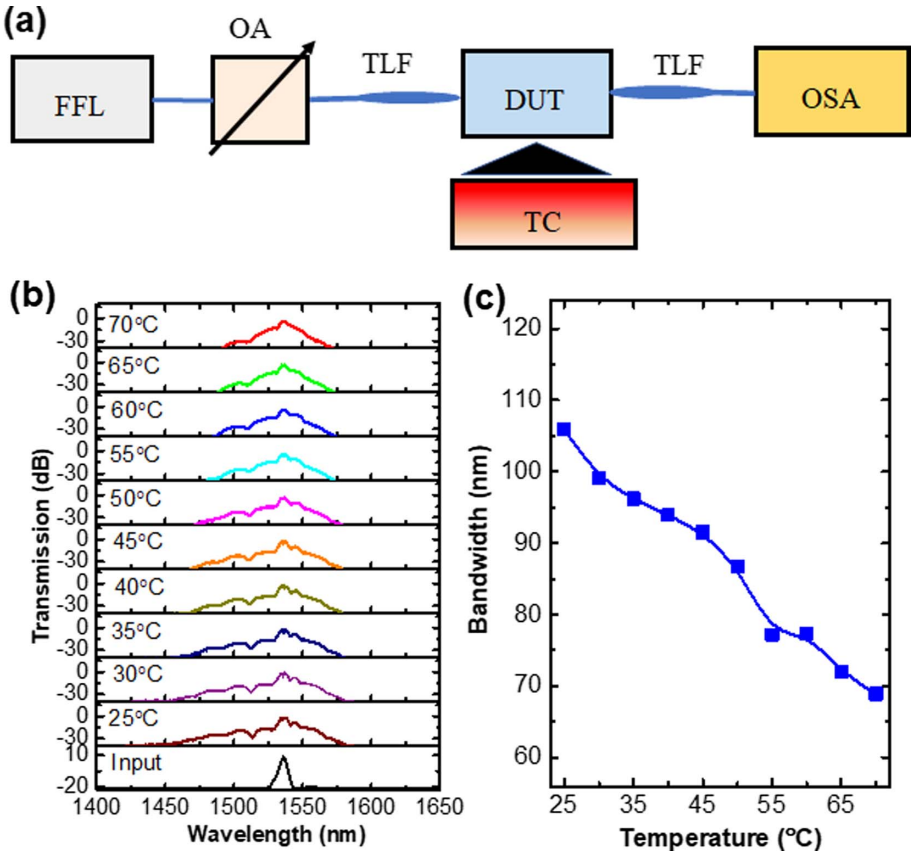

Fig. 5. (a) Schematic of the experimental setup, where blue lines denote the polarization maintaining (PM) fibers, with DUT, device under test; OSA, optical spectrum analyzer; TLF, tapered lensed fiber; TC, temperature controller; OA, optical attenuator; FFL, femtosecond fiber laser. (b) Measured spectral broadening at different temperatures and the input pulse at a fixed input wavelength of 1536 nm. (c) Measured spectral bandwidth at −30 dB level as a function of temperature.

conclusions. The input pulse located at 1536 nm is closest to the grating band edge when the temperature is set to 25°C. As the temperature is increased, the grating band edge experiences a redshift [Fig. 6(a)]. Consequently, the input pulse shifts further away from the high dispersion region located near the blue side of the grating band edge. As the magnitude of dispersion decreases, the soliton period increases [19], and pulses experience a lesser extent of soliton compression and other effects. Therefore, any enhancements from soliton effects in the first stage decrease, and the output spectrum experiences less spectral broadening.

We note further that in the spectral broadening measurement experiment, the pulse-stopband separation at 25°C is 17 nm, chosen to be moderately close to the high dispersion region of the grating band edge, and well within the high-transmission, low-loss wavelength region. If the source pulses are wavelength tuned to be even closer to the stopband, the dispersion experienced by the pulses will be considerably larger, and greater spectral broadening is expected from more extensive soliton effects, particularly through the formation of and fission of solitons, and may further enhance the spectral broadening. The results further confirm that the pulse-stopband detuning governs the dispersive strength experienced by an optical field and in turn influences the extent of nonlinear interactions occurring in the nonlinear grating.

In general, both the thermo-optic effect (whereby a change in temperature results in a change in the bulk refractive index of a material) and thermal expansion may cause a change in the grating stopband ($\Delta\lambda_B$) when a temperature change ΔT is applied according to the equation $\Delta\lambda_B = \lambda_B(1/n_{\text{eff}} \times \mathrm{d}n_{\text{eff}}/\mathrm{d}T + \alpha_T)\Delta T$, where we denote λ_B and n_{eff} as the center wavelength of the stopband and effective index at 25°C, and $\mathrm{d}n_{\text{eff}}/\mathrm{d}T$ and α_T are the thermo-optic and thermal expansion coefficients, respectively. A positive thermo-optic coefficient and thermal expansion coefficient will contribute to a redshift in the stopband when the temperature is increased. In silicon, it has previously been shown that the thermo-optic effect is 2 orders of magnitude larger than the thermal expansion coefficient and is hence the dominant effect [20,21].

To obtain the thermo-optic coefficient of the USRN, we assume the thermo-optic coefficient dominates. We extract the Bragg wavelength (λ_B) at each temperature from the temperature-dependent stopband shown in Fig. 6(a). The results are summarized and plotted in Fig. 6(c). These results allow us to extract the thermo-optic coefficient of the USRN. We expect that contributions to the redshift of the Bragg grating stopband will be dominated by the thermo-optic effect and less by effects from thermal expansion in the grating. The Bragg condition $\lambda_B = 2n_{\text{eff}}\Lambda$ governs the location of the grating stopband, where the grating pitch Λ of the USRN device is 332 nm.

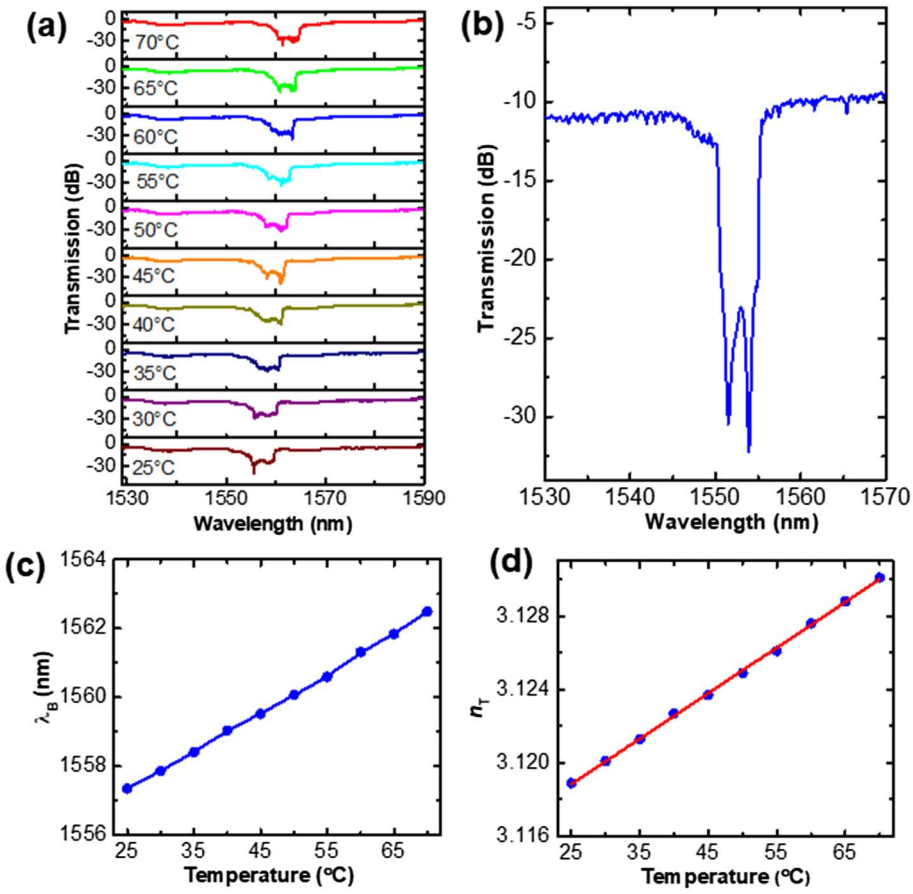

Fig. 6. (a) Measured temperature-dependent stopband of a characteristic cladding modulated Bragg grating with a stopband centered at 1557 nm at 25°C. (b) Measured transmission spectra of USRN grating used in the spectral broadening measurement showing the stopband of 1553 nm at 25°C. (c) The measured Bragg wavelength at different temperatures. (d) The measured refractive index of USRN at different temperatures.

The effective index n_{eff} at 25°C was first calculated using the finite element method, using the experimentally measured value of λ_B and the experimentally obtained refractive index n_T of USRN at this temperature. Using the Bragg condition, measured λ_B, and Λ, we may then extract the effective index n_{eff} at each temperature. And finally, the refractive index n_T of USRN at each temperature can be obtained with the finite element method using measured λ_B and the effective index n_{eff} at each temperature. The experimentally measured λ_B and n_T as a function of temperature are shown in Figs. 6(c) and 6(d), respectively. By fitting the slope of the curve in Fig. 6(d), we obtained the thermo-optic coefficient of USRN. The extracted value is calculated to be 2.48×10^{-4}°C^{-1}, which is an order of magnitude larger than that of stoichiometric silicon nitride [22].

4. DISCUSSION AND CONCLUSIONS

Table 1 compares our approach with other pulse bandwidth tuning methods. As listed in Table 1, the spectral bandwidth of an optical pulse may be tuned using acousto-optic filters [3,4], strain-induced fiber Bragg gratings [5], electro-optic modulators [6], and resonant filters [7–9]. However, due to the involved spectral truncation by band-pass filtering of the pulse, the power losses of these methods are very high. For example, a power loss close to 20 dB (excluding coupling losses) was reported in Refs. [3,7]. By comparison, the laser tuning in this work only has an device insertion loss of 6.35 dB, because no spectral truncation is required in our method. Fiber-waveguide coupling losses in our device are around 2.5 dB per facet. With more advanced packaging techniques, this value could be considerably reduced. In addition to a much lower power loss in our technique, the tuning dynamic range of the optical bandwidths of this work is also much larger, ranging from 69 to 106 nm compared to <4 nm in previous work. The lower power loss and broader bandwidth tuning dynamic range make the thermo-optic tuning method in our work highly advantageous for low-loss laser pulse bandwidth tuning.

The demonstrated thermal tunability of output pulse spectra is a new way to control the pulse properties while conserving the pulse energy. Importantly, the pulses operate in the wavelength region of the CMBG where the transmission is high. In pulsed fiber lasers, which are popular for short-pulse delivery, the temporal pulse widths are changed by applying band-pass filters. In this two-stage device, the spectral bandwidth may be temperature tuned with the majority of spectral broadening occurring in the nonlinear waveguide stage after the cladding-

Table 1. Comparison of Various Approaches toward Tuning of Laser Pulse Bandwidth

Method	Power Loss	30 dB Bandwidth Range	Refs.
Acousto-optic tunable filter	**17 dB**	**<2 nm**	[3][a]
Acousto-optic tunable coupler based on an acousto-optic filter and a taper fiber	Not mentioned	**<2 nm**	[4][a]
Strain-induced chirped fiber Bragg grating and erbium-ytterbium co-doped fibers	Not mentioned	**<1 nm**	[5][a]
Integrated **electroabsorption modulator**	Not mentioned	**<1 nm**	[6][a]
Optical band-pass filter based on **thermal-tuning** microring-MZI structure	**15 dB**	**<4 nm**	[7][a]
Compact microring resonators using **thermally tuned** interferometric couplers	Not mentioned	**<1 nm**	[8][a]
Add-drop filter using a **voltage-tuned** microtoroidal resonator	Not mentioned	**<1 nm**	[9][a]
Using **temperature tunable** USRN grating	**6.35 dB**	**69–106 nm**	**This work**

[a]Denotes a method that utilizes spectral truncation of the pulse spectrum to tune the pulse bandwidth. In these methods, the energy loss increases as the tuning of the pulse bandwidth is decreased.

apodized modulated Bragg grating. In this second stage, nonlinear effects dominate. To further refine the pulses that are derived from the two-stage system, appropriate dispersion management techniques may be further incorporated into the two-stage design to ensure that pulses exiting from the chip will be close to transform limited.

Furthermore, the approach introduced here may be combined in the future with on-chip tuning mechanisms including integrated microheaters, which may bring about another dimension of tunability in the grating dispersion. Aside from applying a constant thermal effect to the entire grating device, the application of thermal gradients [23] in gratings may also unlock the ability to achieve advanced optical waveform manipulation functions that leverage Bragg soliton effects [24,25], enabling interesting new on-chip optical signal processing techniques.

We have demonstrated a new method for spectral bandwidth tuning of laser pulses. The method provides a high dynamic tuning range for the bandwidth while minimizing loss in pulse energy associated with spectral truncation. Contrary to other approaches for pulse bandwidth tuning, this approach does not require filtering out unwanted spectral components but rather uses the Kerr nonlinearity to selectively extend or reduce the pulse spectrum. The large thermo-optic coefficient of USRN (10× larger than in Si_3N_4) further facilitates temperature tuning of the output pulse bandwidth using a nonlinear USRN grating. The experimental results confirm the dependence of the output pulse bandwidth on the relative location of the Bragg grating band edge that arises from the positive thermo-optic coefficient of the USRN. The results are further facilitated by the high nonlinear refractive index and absence of two-photon absorption of the USRN at telecommunications wavelengths [26,27]. The approach leverages rich Bragg soliton dynamics [28–30], which has previously been demonstrated for on-chip supercontinuum enhancement and observation of Bragg soliton fission [17,31], and provides a new avenue to achieve on-chip tuning of a laser pulse spectrum with minimal losses in pulse energy.

Funding. National Research Foundation Competitive Research Grant (NRF-CRP18-2017-03); Ministry of Education ACRF Tier 2 Grant.

Disclosures. The authors declare no conflicts of interest.

REFERENCES

1. Z. Jiang and X.-C. Zhang, "Single-shot spatiotemporal terahertz field imaging," Opt. Lett. **23**, 1114–1116 (1998).
2. R. Knappe, "Applications of picosecond lasers and pulse-bursts in precision manufacturing," Proc. SPIE **8243**, 82430I (2012).
3. D. A. Smith, M. W. Maeda, J. J. Johnson, J. S. Patel, M. A. Saifi, and A. Von Lehman, "Acoustically tuned erbium-erbium-doped fiber ring laser," Opt. Lett. **16**, 387–389 (1991).
4. L. Huang, X. Song, P. Chang, W. Peng, W. Zhang, F. Gao, F. Bo, G. Zhang, and J. Xu, "All-fiber tunable laser based on an acousto-optic tunable filter and a tapered fiber," Opt. Express **24**, 7449–7455 (2016).
5. J. Yang, S. Tjin, and N. Q. Ngo, "Wideband tunable linear-cavity fiber laser source using strain-induced chirped fiber Bragg grating," Opt. Laser Technol. **36**, 561–565 (2004).
6. B. Mason, G. A. Fish, S. P. DenBaars, and L. A. Coldren, "Widely tunable sampled grating DBR laser with integrated electroabsorption modulator," IEEE Photon. Technol. Lett. **11**, 638–640 (1999).
7. Y. Ding, M. Pu, L. Liu, J. Xu, C. Peucheret, X. Zhang, D. Huang, and H. Ou, "Bandwidth and wavelength-tunable optical bandpass filter based on silicon microring-MZI structure," Opt. Express **19**, 6462–6470 (2011).
8. L. Chen, N. Sherwood-Droz, and M. Lipson, "Compact bandwidth-tunable microring resonators," Opt. Lett. **32**, 3361–3363 (2007).
9. J. Yao and M. C. Wu, "Bandwidth-tunable add–drop filters based on micro-electro-mechanical-system actuated silicon microtoroidal resonators," Opt. Lett. **34**, 2557–2559 (2009).
10. V. Liu, Y. Jiao, D. A. B. Miller, and S. Fan, "Design methodology for compact photonic-crystal-based wavelength division multiplexers," Opt. Lett. **36**, 591–593 (2011).
11. M. R. Paiam and R. I. MacDonald, "Design of phased-array wavelength division multiplexers using multimode interference couplers," Appl. Opt. **36**, 5097–5108 (1997).
12. J. E. Carlstrom, R. L. Plambeck, and D. D. Thornton, "A continuously tunable 65–15-GHz Gunn oscillator," IEEE Trans. Microw. Theory Tech. **33**, 610–619 (1985).
13. K. L. Vodopyanov, J. P. Maffetone, I. Zwieback, and W. Ruderma, "$AgGaS_2$ optical parametric oscillator continuously tunable from 3.9 to 11.3 μm," Appl. Phys. Lett. **75**, 1204–1206 (1999).
14. G. P. Agrawal, *Nonlinear Fiber Optics* (Elsevier Science, 2013).
15. B. U. Sohn, J. W. Choi, D. K. T. Ng, and D. T. H. Tan, "Optical nonlinearities in ultra-silicon-rich nitride characterized using z-scan measurements," Sci. Rep. **9**, 10364 (2019).
16. J. W. Choi, B. U. Sohn, G. F. R. Chen, D. K. T. Ng, and D. T. H. Tan, "Soliton-effect optical pulse compression in CMOS-compatible ultra-silicon-rich nitride waveguides," APL Photon. **4**, 110804 (2019).
17. E. Sahin, A. Blanco-Redondo, P. Xing, D. K. T. Ng, C. E. Png, D. T. H. Tan, and B. J. Eggleton, "Bragg soliton compression and fission on CMOS-compatible ultra-silicon-rich nitride," Laser Photon. Rev. **13**, 1900114 (2019).
18. T. Wang, D. K. T. Ng, S. K. Ng, Y. T. Toh, A. K. L. Chee, G. F. R. Chen, Q. Wang, and D. T. H. Tan, "Supercontinuum generation in bandgap engineered, back-end CMOS compatible silicon rich nitride waveguides," Laser Photon. Rev. **9**, 498–506 (2015).

19. C. M. Chen and P. L. Kelley, "Nonlinear pulse compression in optical fibers: scaling laws and numerical analysis," J. Opt. Soc. Am. B **19**, 1961–1967 (2002).
20. T. Middelmann, A. Walkov, G. Bartl, and R. Schödel, "Thermal expansion coefficient of single-crystal silicon from 7 K to 293 K," Phys. Rev. B **92**, 174113 (2015).
21. B. J. Frey, D. B. Leviton, and T. J. Madison, "Temperature-dependent refractive index of silicon and germanium," Proc. SPIE **6273**, 62732J (2006).
22. A. Arbabi and L. L. Goddard, "Measurements of the refractive indices and thermo-optic coefficients of Si_3N_4 and SiO_x using microring resonances," Opt. Lett. **38**, 3878–3881 (2013).
23. W. Zhang and J. Yao, "A fully reconfigurable waveguide Bragg grating for programmable photonic signal processing," Nat. Commun. **9**, 1396 (2018).
24. G. Lenz and B. J. Eggleton, "Adiabatic Bragg soliton compression in nonuniform grating structures," J. Opt. Soc. Am. B **15**, 2979–2985 (1998).
25. R. E. Slusher, B. J. Eggleton, T. A. Strasser, and C. M. de Sterke, "Nonlinear pulse reflections from chirped fiber gratings," Opt. Express **3**, 465–475 (1998).
26. D. T. H. Tan, K. J. A. Ooi, and D. K. T. Ng, "Nonlinear optics on silicon-rich nitride-a high nonlinear figure of merit CMOS platform," Photon. Res. **6**, B50–B66 (2018).
27. K. J. A. Ooi, D. K. T. Ng, T. Wang, A. K. L. Chee, S. K. Ng, Q. Wang, L. K. Ang, A. M. Agarwal, L. C. Kimerling, and D. T. H. Tan, "Pushing the limits of CMOS optical parametric amplifiers with USRN:Si_7N_3 above the two-photon absorption edge," Nat. Commun. **8**, 13878 (2017).
28. H. G. Winful, "Pulse-compression in optical fiber filters," Appl. Phys. Lett. **46**, 527–529 (1985).
29. B. J. Eggleton, C. M. de Sterke, and R. E. Slusher, "Bragg solitons in the nonlinear Schrodinger limit: experiment and theory," J. Opt. Soc. Am. B **16**, 587–599 (1999).
30. B. J. Eggleton, R. E. Slusher, C. M. de Sterke, P. A. Krug, and J. E. Sipe, "Bragg grating solitons," Phys. Rev. Lett. **76**, 1627–1630 (1996).
31. E. Sahin, A. Blanco-Redondo, D. K. T. Ng, C. E. Png, B. J. Eggleton, and D. T. H. Tan, "Supercontinuum enhancement using Bragg solitons on a CMOS-compatible chip," Proc. SPIE **11026**, 1102607 (2019).